Structural and Electronic Snapshots during the Transition from a Cu(II) to Cu(I) Metal Center of a Lytic Polysaccharide Monooxygenase by X-ray Photoreduction[*]

Mikael Gudmundsson[‡1], **Seonah Kim**[§1], **Miao Wu**[‡1], **Takuya Ishida**[‡¶], **Majid Hadadd Momeni**[‡],
Gustav Vaaje-Kolstad[‖], **Daniel Lundberg**[‡], **Antoine Royant**[**‡‡], **Jerry Ståhlberg**[‡‖], **Vincent G. H. Eijsink**[‖],
Gregg T. Beckham[§2], **and Mats Sandgren**[‡3]

From the [‡]*Department of Chemistry and Biotechnology, Swedish University of Agricultural Sciences, SE-750 07 Uppsala, Sweden, the* [§]*National Bioenergy Center, National Renewable Energy Laboratory, Golden, Colorado 80401, the* [¶]*Department of Biomaterials Sciences, Graduate School of Agricultural and Life Sciences, The University of Tokyo, Tokyo 113-8657, Japan, the* [‖]*Department of Chemistry, Biotechnology and Food Science, Norwegian University of Life Sciences, NO-1432 Ås, Norway, the* [**]*Institut de Biologie Structurale, Université Grenoble Alpes-CNRS-CEA, 38042 Grenoble, France, and the* [‡‡]*European Synchrotron Radiation Facility, 38000 Grenoble, France*

Background: Lytic polysaccharide monooxygenases (LPMOs) exhibit a copper center that binds dioxygen for catalysis.
Results: We present LPMO structures from Cu(II) to Cu(I) and analyze the transition with quantum mechanical calculations.
Conclusion: Reduction changes the copper coordination state but requires only minor structural and electronic changes.
Significance: These structures provide insight into LPMO catalytic activation for further mechanistic studies.

Lytic polysaccharide monooxygenases (LPMOs) are a recently discovered class of enzymes that employ a copper-mediated, oxidative mechanism to cleave glycosidic bonds. The LPMO catalytic mechanism likely requires that molecular oxygen first binds to Cu(I), but the oxidation state in many reported LPMO structures is ambiguous, and the changes in the LPMO active site required to accommodate both oxidation states of copper have not been fully elucidated. Here, a diffraction data collection strategy minimizing the deposited x-ray dose was used to solve the crystal structure of a chitin-specific LPMO from *Enterococcus faecalis* (*Efa*CBM33A) in the Cu(II)-bound form. Subsequently, the crystalline protein was photoreduced in the x-ray beam, which revealed structural changes associated with the conversion from the initial Cu(II)-oxidized form with two coordinated water molecules, which adopts a trigonal bipyramidal geometry, to a reduced Cu(I) form in a T-shaped geometry with no coordinated water molecules. A comprehensive survey of Cu(II) and Cu(I) structures in the Cambridge Structural Database unambiguously shows that the geometries observed in the least and most reduced structures reflect binding of Cu(II) and Cu(I), respectively. Quantum mechanical calculations of the oxidized and reduced active sites reveal little change in the electronic structure of the active site measured by the active site partial charges. Together with a previous theoretical investigation of a fungal LPMO, this suggests significant functional plasticity in LPMO active sites. Overall, this study provides molecular snapshots along the reduction process to activate the LPMO catalytic machinery and provides a general method for solving LPMO structures in both copper oxidation states.

Glycoside hydrolases (GHs)[6] are responsible for significant turnover of recalcitrant polysaccharides such as cellulose, hemicellulose, and chitin in nature and are thus of major importance in the global carbon and nitrogen cycles. GHs are extremely diverse enzymes and have undergone extensive characterization and classification, often driven by their potential utilization in the growing biofuels industry (1–5). More recently, a new class of enzymes was discovered, classified as lytic polysaccharide monooxygenases (LPMOs), which cleave glycosidic linkages in polysaccharides via a copper-mediated, oxidative mechanism (6–12). LPMOs represent a new enzyme mechanism for the decomposition of recalcitrant polysaccharides and act synergistically with traditional hydrolytic enzymes (6, 13–15). Unlike GHs, LPMO action generally does not involve a decrystallization step to detach single polysaccharide chains from their insoluble and often crystalline substrates, a process that requires a substantial amount of thermodynamic work (16–18). Instead, most LPMOs characterized to date are thought to act directly on surfaces of crystalline polysaccharides (6, 19). In this manner, LPMOs are able to synergize with

---

[1] These authors contributed equally to this work.
[2] To whom correspondence may be addressed: National Bioenergy Center, National Renewable Energy Laboratory, 15013 Denver West Pkwy., MS 3322, Golden, CO 80401. Tel.: 303-384-7806; E-mail: gregg.beckham@nrel.gov.
[3] To whom correspondence may be addressed: Dept. of Chemistry and Biotechnology, Swedish University of Agricultural Sciences, 750 07 Uppsala, Sweden. Tel.: 46-18-673179; E-mail: mats.sandgren@slu.se.

[6] The abbreviations used are: GH, glycoside hydrolase; LPMO, lytic polysaccharide monooxygenases; RMSD, root mean square deviation; PDB, Protein Data Bank; CSD, Cambridge Structural Database; CBM, carbohydrate-binding module; AA, Auxiliary Activity; DFT, density functional theory; ASM, active site model.

hydrolytic enzymes because they are hypothesized to make chain breaks in crystalline regions that are typically thought to be inaccessible for endoglucanases. Conversely, an LPMO able to cleave soluble substrates was recently discovered, indicating an increasing diversity in substrate specificities of these enzymes (20).

LPMOs were previously classified as family 33 carbohydrate-binding modules (CBM33s), which range in origin from bacteria to algae, and family 61 glycoside hydrolases (GH61s), which are of fungal origin. CBM33s mined from genomic data often exhibit modular complexity, whereas GH61s are typically either single module enzymes or are bimodular with a catalytic domain and a family 1 CBM (14), similar to many fungal carbohydrate-active enzymes. Recently, Henrissat and co-workers (5) updated the Carbohydrate-Active Enzyme database and classified CBM33s as Auxiliary Activity 10 (AA10) and GH61s as AA9. Another LPMO family was also recently classified as AA11, which exhibits sequence, structural, and electronic characteristics between that of AA9 and AA10 (12).

The chitin-active LPMO from the Gram-negative chitinolytic bacterium *Serratia marcescens*, CBP21, was the first LPMO to be biochemically characterized (6, 21, 22). CBP21 catalysis was shown to be dependent on molecular oxygen, an external electron donor, and the presence of a metal ion cofactor (6), later identified as copper (19). Copper ions have been identified to activate AA10 (19, 23), AA9 (7, 9, 10), and AA11 LPMOs (12). In addition to CBP21, LPMO activity has only been demonstrated for two other CBM33s so far, a cellulose-active CBM33 from *Streptomyces coelicolor* (CelS2 (8)) and a chitin-active CBM33 from *Enterococcus faecalis* (*Efa*CBM33A (24)), the latter of which is the subject of this study. *Efa*CBM33A is the only LPMO found in the genome of *E. faecalis* and constitutes, along with a GH family 18 chitinase (*Efa*Chi18A), the chitinolytic machinery of the bacterium. *E. faecalis* is an opportunistic pathogen, and both *Efa*CBM33A and *Efa*Chi18A are virulence factors (25, 26), suggesting a putative second role for these enzymes beyond biomass depolymerization.

The LPMO active site is constituted by two histidine residues (one of which is the N-terminal residue) that coordinate a copper ion in a motif referred to as the "histidine brace" (6, 7, 10, 27). The copper ion is essential for catalytic activity and is likely to be involved in the activation of molecular oxygen (7, 9, 24). Soluble products resulting from lytic oxidation have been identified as aldonic acids (6, 8–10, 28) or as oligomers with an oxidized nonreducing end sugar, *i.e.* a 4-keto sugar (20, 29), indicating differences in enzyme regioselectivity. The oxidation products were recently definitively confirmed by NMR spectroscopy (20), and some progress has recently been made toward understanding regioselectivity (30). To date, aldonic acids are the only products observed for AA10 and AA11 LPMOs, whereas both aldonic acids and 4-keto sugars have been observed for AA9 enzymes.

The catalytic mechanism of AA9 LPMOs, which to date only are found in fungi, was recently examined with density functional theory (DFT) calculations (11). Kim *et al.* (11) predicted that AA9 LPMOs employ a Cu(II)-oxyl reactive oxygen species for hydrogen abstraction from the substrate, followed by an

oxygen-rebound mechanism for substrate hydroxylation. This step will be followed by an elimination reaction, resulting in glycosidic bond cleavage. To activate the LPMO catalytic cycle, the initial dioxygen binding was hypothesized to require reduction of Cu(II) oxidation state of the enzyme to a Cu(I) state, likely mediated by an enzymatic or small molecule reducing agent.

Until recently, there has been a dearth of structural data for metal binding in AA10 LPMOs compared with fungal AA9 LPMOs. Recently, Hemsworth *et al.* (27) reported the structure of *Bacillus amyloliquefaciens* CBM33 (*Bam*CBM33), with unknown catalytic activity, binding Cu(I). It was shown that *Bam*CBM33 is stabilized in the presence of copper and that the active site of *Bam*CBM33 with a Cu(I) ion adopts a T-shaped geometry (PDB codes 2YOX and 2YOY). A Cu(II) form of *Bam*-CBM33 was not crystallized, but x-ray absorption near edge structure (XANES) and EPR spectroscopic methods were used to demonstrate that the enzyme was readily photoreduced during crystallization from the Cu(II) form to a Cu(I) state (27).

In this study, we investigate the active site of *Efa*CBM33 by progressively photoreducing the catalytic copper from Cu(II) to Cu(I) in the x-ray beam using a data collection minimizing the x-ray dose that is deposited in the sample. During photoreduction, we determine successive structural states by collecting x-ray diffraction data sets on the same crystal. By comparing the structures to known Cu(I) and Cu(II) analogues found in the Cambridge Structural Database (CSD) (31), we ascertain that the obtained structures of the *Efa*CBM33A unambiguously describe varying oxidation states ranging from Cu(II) to Cu(I). Lastly, we conduct quantum mechanical calculations on an active site model of the Cu(II) and Cu(I) forms of *Efa*CBM33, which suggest that the electronic structure of the active site remains quite similar as measured by atomic charges. Because the initial reduction of Cu(II) is likely a requirement for LPMO activity, these results offer a structural and electronic picture of how LPMO active sites are preactivated for oxygen binding and subsequent catalysis.

EXPERIMENTAL PROCEDURES

Protein Preparation and Crystallization of EfaCBM33A— *Efa*CBM33A was expressed and purified as previously described (24). The protein was incubated with 1 mM $CuSO_4$ for 0.5 h. After soaking, the protein solution was desalted using a 10 DG column (Bio-Rad) and concentrated to 25 mg/ml prior to crystallization. *Efa*CBM33A crystals were obtained in 20% (w/v) PEG 8000 and 0.1 M HEPES, pH 7.5, by the sitting drop vapor diffusion method as previously described (24). Rod-shaped crystals grew to an approximate size of 400 × 53 × 40 μm after 2 days of incubation at 20 °C. The crystal used for data collection was soaked in the crystallization solution with the addition of 20% PEG 400 as a cryoprotectant for ~10 s prior to being plunged into liquid nitrogen.

Diffraction Data Collection and Structure Solution—X-ray diffraction experiments were performed at Beamline ID14-EH1 at the European Synchrotron Radiation Facility, Grenoble, France. Six diffraction data sets were collected using the same single crystal. By utilizing a rod-shaped crystal, monitoring the evolution of UV-visible absorption spectra with x-ray dose (32),

TABLE 1

X-ray data collection and processing, structure refinement, and final model statistics

PDB code	4ALC	4ALE	4ALR	4ALQ	4ALS	4ALT
Data quality						
Space group	$P2_12_12_1$	$P2_12_12_1$	$P2_12_12_1$	$P2_12_12_1$	$P2_12_12_1$	$P2_12_12_1$
Cell dimensions (Å)						
a	43.42	43.42	43.42	43.46	43.44	43.40
b	48.56	48.57	48.58	48.62	48.61	48.57
c	68.45	68.46	68.46	68.51	68.50	68.43
Data collections statistics						
Wavelength (Å)	0.9334	0.9334	0.9334	0.9334	0.9334	0.9334
Resolution range (Å)	48.56–1.49	48.57–1.48	39.68–1.49	48.68–1.48	48.61–1.47	39.60–1.49
No. of unique reflections	23,919 (3317)	24,395 (3216)	23,936 (3324)	24,358 (3235)	24,138 (3119)	23,899 (3307)
Multiplicity	3.4 (3.0)	3.4 (2.9)	3.4 (3.0)	3.3 (2.9)	2.9 (2.3)	3.4 (3.1)
Completeness	98.6 (96.1)	97.8 (90.5)	98.6 (96.1)	97.8 (91.2)	96.6 (87.9)	98.6 (95.9)
R_{merge}[a]	0.094 (0.477)[b]	0.096 (0.503)	0.094 (0.484)	0.067 (0.237)	0.056 (0.142)	0.100 (0.564)
Exposure time/frame (s)	1	1	1	3	6	1
Total exposure time (s)	97	194	485	776	1358	1455
Dose (grays)	8.27×10^4	1.65×10^5	2.47×10^5	4.94×10^5	9.86×10^5	1.07×10^6
Refinement						
Resolution range (Å)	39.60–1.49	39.61–1.48	39.62–1.49	39.65–1.48	39.64–1.47	39.60–1.49
Observations	80,452 (10080)	81,915 (9417)	80,300 (10,018)	81,296 (9301)	69,202 (7187)	80,875 (10,226)
No. of reflections used (working set)	22,667	23,130	22,679	23,087	22,872	22,647
R_{work} (%)	16.1	16.1	16.1	15.6	15.6	16.1
R_{free} (%)	18.8	18.4	18.8	18.3	19.6	18.8
No. of residues	167	167	167	167	167	167
No. of water molecules	289	286	282	281	292	280
No. of copper atoms	1	1	1	1	1	1
RMSD bond lengths (Å)	0.008	0.008	0.008	0.008	0.008	0.008
RMSD angles (°)	1.230	1.229	1.230	1.210	1.221	1.242
Ramachandran[c]						
In favored regions (%)	100	100	100	100	100	100
Outliers (%)	0	0	0	0	0	0

[a] $R_{merge} = \Sigma_{hkl}\Sigma_i |I_{-i(hkl)} - <I_{(hkl)}>|/\Sigma_{hkl}\Sigma_i I_{i(hkl)}$.
[b] Values for the highest resolution shell are given in parentheses.
[c] Calculated using a strict boundary Ramachandran definition given by Kleywegt and Jones (41).

and a strategy for helical data collection (33), the radiation dose was minimized, and data of a minimally photoreduced state of *Efa*CBM33 could be collected (34). A helical data collection consists of defining two points on the crystal along the rotation axis of the goniometer. Although the crystal is rotated over a total 97° angular wedge by 1° steps, it is automatically translated along the rotation axis in between two consecutive rotation steps, thus presenting a fresh part of the crystal to the beam for each diffraction frame. Eventually, the x-ray dose deposited in the sample will approximately be d/w smaller than that deposited with a standard data collection protocol, where d is the horizontal distance between the two points, and w is the horizontal width of the beam. Two points on a limited region ($320 \times 53 \times 40\ \mu m$) of the crystal were set up as start and end points for data collection with a 50×100-μm x-ray beam. A different exposure dose per image was used for some data sets, as shown in Table 1. Collecting subsequent data sets by this method allowed for the analysis of the effects of photoreduction on the active site copper with minimal systematic errors, because all data sets were collected from multiple and subsequent exposures of the same crystal volume.

All data sets were indexed and integrated using the program XDS (35) and scaled with the CCP4 program suite version 6.2.0 (36). The structures of *Efa*CBM33A were solved by molecular replacement using CBP21 (22) (PDB code 2BEM) as the starting model. Model building and maximum-likelihood refinement were performed with iterative cycles of model building in COOT version 0.6.2 (37), by inspection of 2*mFo-DFc* and *mFo-DFc* σA-weighted maps, and model refinement in Refmac5 version 5.6.0117 (38). The bound copper ion was modeled in at a

final stage of the refinement. PyMOL 1.5 (39) was used for analysis of the structures and figure preparations. LSQMAN (40) was used for structural alignments, and Ramachandran statistics were determined using MOLEMAN2 (41). Omit maps were calculated using Phenix 1.8.1 (42). Dose calculations for the exposed crystal regions were performed using RADDOSE version 2 (43, 44).

Crystallographic Database Search—A search of the Cambridge Structural Database was performed using ConQuest 1.14. Detailed search parameters are described below in the text.

Quantum Mechanical Calculations—Quantum mechanical calculations based on DFT were performed using Gaussian09 (45) on an active site model (ASM) of *Efa*CBM33, which includes His[29], Glu[64], Ala[112], His[114], Trp[176], Ile[178], Phe[185], and the copper ion. The crystallographic water molecules that coordinate the copper ion were also included where appropriate. Smaller and larger ASMs were considered (data not shown), and this model was found to provide the optimal balance between reproducing the crystal structure and being computationally tractable. Additionally, as reported under "Results," the RMSDs of the resulting models of both the Cu(II) and Cu(I) states were below 0.4 Å, a value that is well within the range considered to represent sufficient accuracy in cluster models of enzyme active sites (46). All geometry optimizations were conducted with the local meta-GGA M06-L functional (47, 48) and the 6−31G(d) basis set for all atoms. M06-L was chosen because of improved accuracy for the dispersive and mixed binding complexes. The local density function is computationally efficient for optimization of large structures, employing thousands
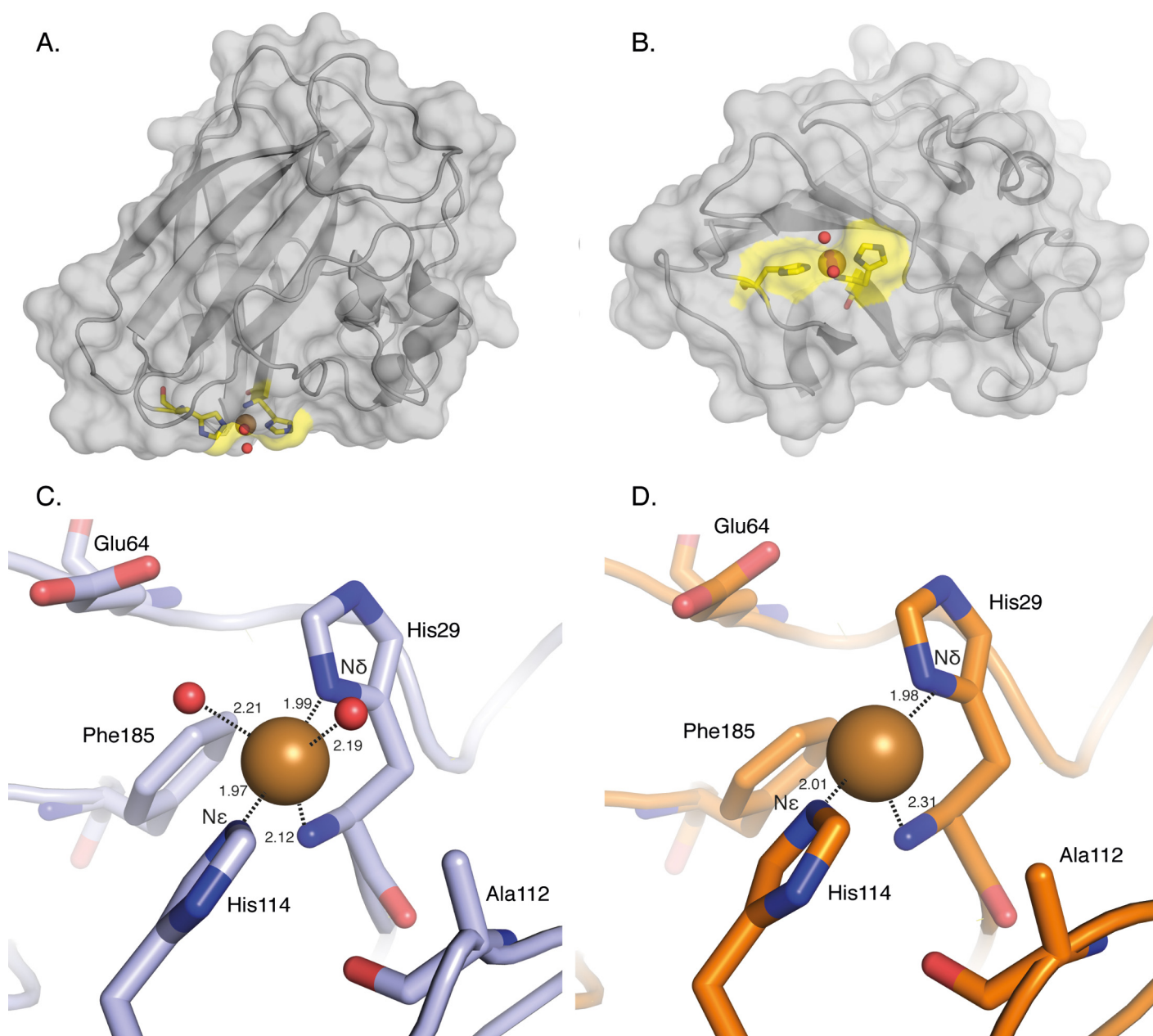
FIGURE 1. **Overall structure of *Efa*CBM33.** *A* and *B*, side (*A*) and bottom (*B*) views of the crystal structure of Cu(II)-bound *Efa*CBM33A with a cartoon and transparent surface model in *gray* (PDB code 4ALC; the structure with the lowest radiation dose). The active center is highlighted in *yellow*, and the two residues making up the histidine brace are shown in stick format. The copper atom is shown as a *brown sphere*, and two water molecules coordinated to the copper are shown as *red spheres*. *C*, the active site in the oxidized (Cu(II)) form of *Efa*CBM33 (PDB code 4ALC). Note that there are not other stabilizing interactions between the two coordinating water molecules and the enzyme. *D*, the active site in *Bam*CBM33 binding Cu(I) (PDB code 2YOX) (27). Distances to the copper ion are provided in Å.

of basis functions. All α- and β-carbons were fixed during optimizations. All systems were treated with the conductor-like polarizable continuum model (49, 50) using diethyl ether solvation ($\epsilon = 4$ for the protein environment) (51). We computed the harmonic vibrational frequencies for all optimized structures to confirm that they are minima, possessing zero imaginary frequencies. Atomic charges were calculated using natural population analysis from NBO 6.0.

RESULTS

Overall Structure of EfaCBM33A in Complex with Copper— The *Efa*CBM33A with a bound copper atom was crystallized in

space group $P2_12_12_1$ with cell dimensions of $43.4 \times 48.6 \times 68.5$ Å, one protein molecule per asymmetric unit, and a V_m (Matthews coefficient) (53) of 1.97 Å^3/Da including all Cα atoms in the structure. We present six structures of *Efa*CBM33A along the process of x-ray induced photoreduction, all refined at 1.5 Å and final R and R_{free} values of 15.6–16.1% and 18.3–19.6%, respectively. The data collection and refinement statistics are summarized in Table 1. In all the structure models, there is clear electron density for all the 169 amino acid residues, ~285 water molecules, and 1 copper atom bound to the protein. Negligible pairwise RMSD values of 0.03–0.04 Å over all protein atoms show that the structures are essentially identical. The

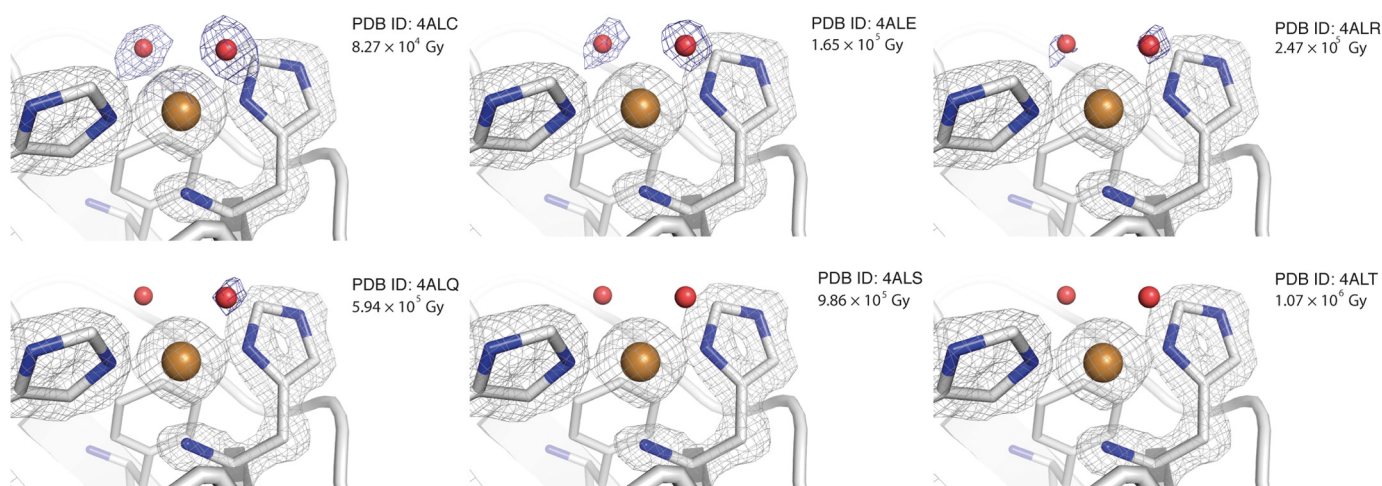# Transition from a Cu(II) to Cu(I) Metal Center of a LPMO

FIGURE 2. **Close up view of the catalytic centers of *Efa*CBM33A at different levels of x-ray exposure.** The *blue* omit-calculated $2mF_o - F_c$ maps (52) are contoured at 0.87 e/Å³, the *gray* $2F_o - F_c$ maps are contoured at 0.89 e/Å³. The *red* oxygen-atom coordinates are taken from the 4ALC structure, are placed throughout the series for reference, and were not used in the calculation of the $2mF_o - F_c$ omit maps. The structural images are labeled by the PDB codes and the dose of x-ray exposure.
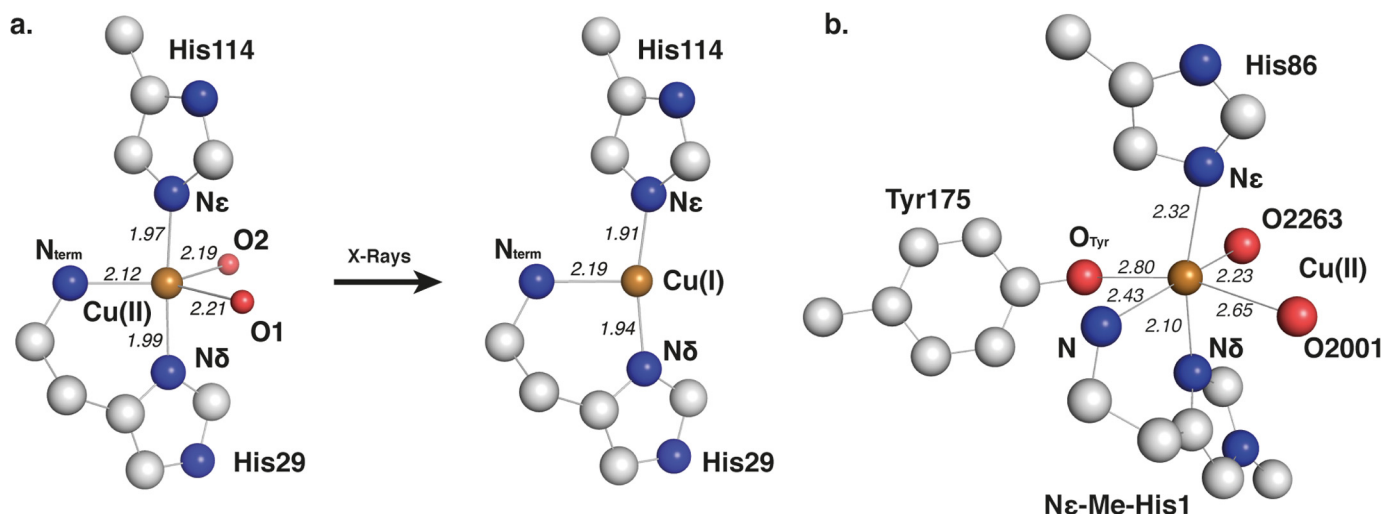

FIGURE 3. **Copper coordination in *Efa*CBM33A and *Tau*GH61A.** Important residues, atoms, and coordination distances to the copper ion in Å. are indicated where appropriate. *a*, the copper binding site of *Efa*CBM33A (PDB code 4ALC) displays a trigonal bipyramidal (*tbp*) coordination of copper and after x-ray exposure adopts a T-shaped (*Tsh*) configuration (PDB code 4ALT). *b*, an octahedral Cu(II) coordination in the GH61A from *T. aurantiacus* (PDB code 2YET). In most AA10 LPMOs, including *Efa*CBM33A, the tyrosine residue labeled *Tyr175* is replaced by phenylalanine.

primary differences are found in the coordination geometry of the copper ion as a function of the x-ray dose. With the exception of the active site, the structure of the copper-bound *Efa*CBM33A herein is very similar to the previously published apo form without copper (PDB code 4A02 (24); 0.54 Å RMSD on Cα atoms).

The overall structure and the active site of *Efa*CBM33A, as observed in the structure determined from the data set obtained after the lowest radiation dose (PDB code 4ALC) exhibits a trigonal bipyramidal (*tbp*) structure coordinated by two conserved histidine residues (the histidine brace) and two water molecules (Fig. 1, A–C). In this configuration, the N-terminal histidine (His[29]) forms a bidentate coordination to the copper ion wherein the backbone N atom occupies one of the three equatorial coordination positions, and the side chain Nδ atom occupies one axial position. The other axial position is occupied by the Nε atom in the His[114] residue. The remaining equatorial positions are occupied by two water molecules.

Three additional residues conserved in AA10 LPMOs are shown in Fig. 1*C*, Glu[64], Ala[112], and Phe[185]. Ala[112] is not conserved in AA9 LPMOs and is thought to play a role in the potential mechanistic differences between AA9 and AA10 LPMOs (27, 54). Phe[185] is located in a similar position to a conserved tyrosine in AA9 LPMOs, which in the latter case therein imparts an octahedral coordination state around the Cu(II) ion (7, 13, 28, 55, 56). In AA9 LPMOs, the Glu[64] residue is replaced by a conserved glutamine residue. The 4ALC data set shows two spherical electron densities (1.93 and 1.91 e/Å³, respectively) at 2.21 and 2.19 Å from the copper ion, which were modeled and refined as water molecules and are shown as *red spheres* in Fig. 1*C*. For the water molecules bound to copper, there are no other stabilizing interactions with the enzyme. Thus, the positions of the water molecules are primarily dictated by coordination to the copper ion.

The only other known AA10 structure with a copper ion bound reported to date is *Bam*CBM33 from Hemsworth *et al.*

TABLE 2

Copper structures with similar coordination as EfCBM33A subjected to the lowest radiation dosage (4ALC)

Structures found in the CSD criteria described in the text listed by their code, oxidation state, bond lengths [Cu–N, unless noted], bond angle distribution, and configuration. All structures include a five-coordinated copper(II) ion, including NIDHOY (which is mislabelled in the CSD). One structure shows a copper configuration that is very similar to the configuration in 4ALC: ZUBHOT (*tbp* configuration with two equatorial oxygen atoms with the longest bond distances to the oxygen from the copper ion), whereas CISHIW also has the same general layout (highlighted in peach). When comparing individual bond distances, it should be noted that both ZUBHOT and CISHIW coordinate to one anionic species each, ClO_4^- and NCS^-, respectively. *sqpy*, square pyramidal; *tbp*, trigonal bipyramidal; *dist.*, distorted. The 4ALC structural details are included for reference at the end of the table (highlighted in turquoise).

CSD code	ox.	bond lengths/Å	bond angle distribution/°	configuration
BUDHEO	Cu^{2+}	1.991, 1.992, 1.993 (Cu-O), 2.025, 2.314 (Cu-O)	87-99, 170-176	*sqpy*
IBUYIP	Cu^{2+}	1.976 (Cu-O), 1.996, 1.998, 2.011, 2.298 (Cu-O)	89-96, 170-174	*sqpy*
WASNOU	Cu^{2+}	1.974 (Cu-O), 1.996, 1.998, 2.009, 2.311 (Cu-O)	89-96, 170-172	*sqpy*
NIDHOY	Cu^{2+}	1.977 (Cu-O), 1.982 (Cu-O), 1.988, 2.015, 2.249	87-102, 168-169	dist. *sqpy*
EDAMAY	Cu^{2+}	1.958 (Cu-O), 1.960 (Cu-O), 1.982, 1.984, 2.346	87-105, 163-167	dist. *sqpy*
HEHTIX	Cu^{2+}	1.919 (Cu-O), 1.970 (Cu-O), 1.983, 2.014, 2.216	86-102, 160-168	dist. *sqpy*
SAWKOS	Cu^{2+}	1.949, 1.953 (Cu-O), 2.028 (Cu-O), 2.041, 2.287	84-97, 157-173	dist. *sqpy*
CISHIW	Cu^{2+}	1.990, 2.034, 2.043, 2.077 (Cu-O), 2.079 (Cu-O)	85-102, 109-139, 159	dist. *tbp*
WASNUA	Cu^{2+}	1.966, 1.989, 2.016 (Cu-O), 2.087, 2.268 (Cu-O)	88-94, 91-145, 176	*tbp*
ZUBHOT	Cu^{2+}	1.953, 1.959, 2.021 (Cu-O), 2.104 (Cu-O), 2.333 (Cu-O)	87-95, 114-126, 171	*tbp*
PDB code	**ox.**	**bond lengths/Å**	**bond angle distribution/°**	**config.**
4ALC	Cu^{2+}	1.97, 1.99, 2.12, 2.19 (Cu-O), 2.21 (Cu-O)	83-94, 131-135	*tbp*

(27), wherein all copper ions were photoreduced to a Cu(I) oxidation state. The *Bam*CBM33 enzyme active site is illustrated in Fig. 1*D*. The coordination geometry therein is in a T-shaped (*Tsh*) geometry with no water molecules coordinated to the copper ion. The corresponding protein-copper interactions retain the structure of the histidine brace. The difference in observed geometry between the 4ALC structure and the *Bam*-CBM33 structure indicates a difference in copper oxidation state, as described in detail further below.

Structural Changes Induced by X-ray Photoreduction—The structural changes caused by the increase in x-ray dosage during photoreduction were limited to the local environment of the copper ion (Fig. 2). Omit map analysis of the copper-coordinated water molecules shows a continuous decay of electron density correlated with x-ray exposure, and at ~1 megagray accumulated radiation (4ALT), both water molecules are completely lost. The electron density for the water molecule closest to Ala[112] is retained slightly longer than the other. The decay of the electron density for the two water molecules coordinated to the copper represents a change in the fraction of Cu(II) to Cu(I) populations between the six structures, as a result of the accumulated radiation dose of the exposed crystal region used for data collection. The structures obtained at higher doses of x-ray radiation reveal a continuous shift in the copper coordination configuration from *tbp* coordination to *Tsh* geometry in the structures that lack the copper-bound water molecules (Fig. 2).

LPMO Copper Oxidation State Determination by Analogy to Small Molecule Copper Complexes—To monitor the reduction of the copper ion bound to *Efa*CBM33A, UV-visible microspectrophotometry was used to record spectral changes of the crystal during x-ray exposure. However, the high background noise

and low copper ion concentration in the sample prevented successful application of this method. Thus, to ascertain whether the x-ray-induced changes in the conformation of the copper site are indicative of an actual reduction of the copper ion from Cu(II) to Cu(I), the CSD was searched for relevant copper structures (31). The copper coordination in the retrieved structures was then compared with the initial and final *Efa*CBM33A structures.

The most obvious structural change upon x-ray exposure is that the two water molecules coordinating to the copper ion gradually disappear, as shown in Fig. 2. This demonstrates that the coordination number for the copper ion drops from five to three; the conformation of the copper site changes from a five-coordinated *tbp* structure to a three-coordinated *Tsh* geometry (Fig. 3). Gradual disappearance of electron density upon increasing the x-ray dosage was not observed for any other water molecule in the structure, suggesting that the effects seen for the copper-bound waters relates to a change in the copper ion. Among more than 40,000 copper structures in the CSD (31), nearly half fit our initial search criteria (1 ≤ coordination number ≤ 8; only nitrogen and/or oxygen as coordinating atoms), including 9,727 five-coordinate and 564 three-coordinate structures (data not shown). Limiting the search to only include those with histidine-like coordination surroundings and excluding strained structures left 10 five-coordinate structures, all Cu(II) (Table 2), and 24 three-coordinate structures, all Cu(I) (Table 3). Details regarding their Cu–N/O bonds, bond angles, torsion angles, and the resulting overall geometry of the copper site are shown in Tables 2 and 3, respectively.

The *Efa*CBM33 structures have two axial copper-nitrogen (Cu–N_{ax} and Cu–$N_{ax'}$) bond distances, which both decrease by

TABLE 3

Copper structures with similar coordination as EfCBM33A after being subjected to radiation

Copper structures with similar coordination as EfCBM33A after being subjected to radiation, using the criterion described in the text as listed in CSD by their code, oxidation state, bond lengths, maximum N–Cu–N bond angle deviation (from 120°), maximum Cu–N–N–N torsion angle, and assigned configuration. All structures include three-coordinate copper(I) ions. One structures has nearly identical configuration to the irradiated form of EfCBM33A (4ALT): PIVNOX (*Tsh*, uneven bond distribution), whereas GUVLUF also has the same general layout (highlighted in peach). *trig*, trigonal; *tpy*, trigonal pyramidal; *Tsh*, T-shaped. pt1 and pt2 denote part 1 and part 2 of the same reported structure, denoting crystallographically independent atoms. The 4ALT structural details are included for reference at the end of the table (highlighted in turquoise).

CSD code	ox.	bond lengths/Å	max bond angle dev./°	max. tors. angle/°	config.
VIQZEA	Cu⁺	1.990, 2.001, 2.002	1	8.4	*trig*
PATVEL	Cu⁺	1.912, 1.960, 1.977	2	3.8	*trig*
QURZEJ	Cu⁺	1.944, 1.970, 1.998	4	0.6	*trig*
QURZAF	Cu⁺	1.947, 1.965, 1.999	6	0.2	*trig*
NERTUA	Cu⁺	1.944, 1.965, 1.969	12	8.5	*trig*
CINWIG,pt1	Cu⁺	1.943, 1.958, 1.952	13	2.9	*trig*
BIZKOL	Cu⁺	1.947, 1.964, 2.021	15	2.3	*trig*
CINWIG,pt2	Cu⁺	1.929, 1.955, 1.983	15	2.2	*trig*
YUYBAW	Cu⁺	1.945, 1.966, 2.125	21	0.8	*trig*
YUYBEA	Cu⁺	1.946, 1.970, 2.122	21	0.6	*trig*
QORHAG	Cu⁺	1.912, 1.921, 2.082	23	2.9	*trig*
DUHHOE,pt1	Cu⁺	1.913, 1.959, 2.042	24	3.6	*trig*
GODVOL	Cu⁺	1.934, 1.999, 2.012	26	0.0	*trig*
GODWAY	Cu⁺	1.913, 1.999, 2.003	28	1.5	*trig*
NIDHUE,pt1,2	Cu⁺	1.998, 1.944, 2.024	28	9.2	*trig*
GODVUR	Cu⁺	1.927, 2.002, 2.024	29	1.4	*trig*
DUHHOE,pt2	Cu⁺	1.935, 1.916, 2.049	31	6.4	*trig*
GUCKIZ	Cu⁺	2.008, 2.016, 2.017	3	14.4	*tpy*
GUCKUL	Cu⁺	1.981, 1.997, 2.009	4	15.0	*tpy*
GUCKEV	Cu⁺	2.049, 2.071, 2.092	17	31.3	*tpy*
VIQZIE	Cu⁺	1.956, 1.987, 2.021	19	11.0	*tpy*
NIDGUD	Cu⁺	1.950, 2.008, 2.034	28	10.2	*tpy*
PIVNOX	Cu⁺	1.898, 1.899, 2.213	45	2.2	*Tsh*
GUVLUF	Cu⁺	1.875, 1.867, 2.287	50	1.2	*Tsh*
PDB code	**ox.**	**bond lengths/Å**	**max. bond angle dev./°**	**max. tors. angle/°**	**config.**
4ALT	Cu⁺	1.81, 1.94, 2.19	47	2.6	*Tsh*

0.05 Å going from *tbp* to *Tsh*, whereas the equatorial copper-nitrogen (Cu–N$_{eq}$) bond distance becomes 0.075 Å longer. Additionally, the nearly linear N$_{ax}$–Cu–N$_{ax'}$ angle in *tbp*, 176.2°, bends a bit off-axis in *Tsh*, 167.5°, whereas the N$_{eq}$–Cu–N$_{ax}$ and N$_{eq}$–Cu–N$_{ax'}$ angles increase by 5.6 and 3.1°, respectively. The five-coordinated form is almost identical to the Cu(II) structure reported by Casella *et al.* (57) (CSD code ZUBHOT), whereas the three-coordinated counterpart most closely mimics the *Tsh* copper(I) structure reported by Sorrell *et al.* (58) (CSD code PIVNOX). A CSD search for five-coordinated, dihydrate copper structures also coordinated by three nitrogen atoms, returned seven structures—all Cu(II)—with several *tbp* examples similar to the hydrated version of *Efa*CBM33A seen in 4ALC (Table 4). Taken together, these observations show that the structural changes observed upon irradiation of *Efa*CBM33A reflect photoreduction of Cu(II) to Cu(I).

Quantum Mechanical Calculations of the LPMO Active Site—The structures presented above enable DFT calculations to quantify how the electronic structure of the active site changes upon reduction. The active sites of 4ALC, the Cu(II) structure, and 4ALT, the Cu(I) structure, were both examined

with the M06-L functional and the 6–31G(d) basis set, by employing an ASM representation of the system. Quantum mechanical geometry optimizations were conducted with a range of ASMs. The model consisting of the residues His[29], Glu[64], Ala[112], His[114], Trp[176], Ile[178], and Phe[185] was found to yield the smallest RMSD values for a size that was still computationally tractable with a full quantum mechanical treatment of the ASM in both structures (Table 5; RMSDs of 0.37 and 0.32 Å for 4ALC and 4ALT, respectively). Fig. 4 shows comparisons between the crystal structures and the quantum mechanically optimized ASMs. All computed distances between coordinating nitrogen atoms and the copper differ from the crystallographically observed distances by less than 0.07 Å, which is well within the resolution of the structure (Table 5).

Subsequent to the geometry optimizations, natural population analysis was conducted to examine the charge distributions for both states. As shown in Table 5, the copper ion charges in the oxidized and reduced states of the active site are +1.48 and +0.99, respectively. These values agree well with the formal oxidation states of Cu(II) and Cu(I) and also agree remarkably well with the charges found in both the formal Cu(II) and Cu(I) oxidation states of +1.48 and +0.92, respec-

TABLE 4

Five-coordinated, dihydrate copper structures in the CSD

Entries selected that exhibit two coordinating water molecules are listed by their CSD code, oxidation state, bond distances, and overall configuration. Notably, the mean Cu–N bond distance is shorter than the mean Cu–O distance. Two copper sites exhibit *sqpy* configuration (highlighted in red), but most are in a *tbp* configuration, as also observed in 4ALC. *sqpy*, square pyramidal; *tbp*, trigonal bipyramidal; *dist.*, distorted; *ax*, axial; *eq*, equatorial.

CSD code	ox.	d(Cu-N)/Å d(Cu-OH$_2$)/Å	config.
DALRUF	Cu^{2+}	1.998/2.006/2.010 2.091/2.102 (H$_2$O)	*sqpy* (O$_{ax}$)
ECUWOP	Cu^{2+}	1.983/1.993/2.023 2.076/2.226 (H$_2$O)	*tbp* (O$_{eq}$)
KAHGAB	Cu^{2+}	1.991/1.995/2.088 2.045/2.224 (H$_2$O)	*tbp* (O$_{eq}$)
LOYXUS	Cu^{2+}	1.994/1.999/2.118 2.019/2.028 (H$_2$O)	dist. *sqpy* (O$_{eq}$)
LUNWOG	Cu^{2+}	1.904/1.975/1.983 2.094/2.239 (H$_2$O)	*tbp* (O$_{eq}$)
QULXEB	Cu^{2+}	1.971/1.974/1.986 1.943/2.145 (H$_2$O)	dist. *tbp* (O$_{eq}$)
XOKJAJ	Cu^{2+}	1.973/1.982/2.087 2.021/2.170 (H$_2$O)	*tbp* (O$_{eq}$)

PDB code	ox.	d(Cu-N)/Å d(Cu-OH$_2$)/Å	config.
4ALC		1.97/1.99/2.12 2.19/2.21 (H$_2$O)	*tbp* (O$_{eq}$)

TABLE 5

Structural and electronic parameters for the ASM (active site model) of 4ALC and 4ALT

NA, not applicable.

	4ALC	4ALC$_{opt}$[a]	4ALT	4ALT$_{opt}$[a]
Cu-Nδ (His^{29}) (Å)	1.990	1.983	1.939	1.977
Cu-N (His^{29}) (Å)	2.118	2.065	2.193	2.177
Cu-Nε (His^{114}) (Å)	1.966	1.994	1.913	1.982
Cu–O1 distances (Å)	2.207	2.220	NA	NA
Cu–O$_2$ distances (Å)	2.189	2.116	NA	NA
Nδ (His^{29}) charge[b]	NA	−0.68	NA	−0.71
N (His^{29}) charge[b]	NA	−0.98	NA	−1.01
Nε (His^{114}) charge[b]	NA	−0.67	NA	−0.68
RMSD (Å)[c]	NA	0.37	NA	0.32
Coordination geometry	*tbp*	*tbp*	*Tsh*	*Tsh*

[a] The "opt" subscript denotes the geometry-optimized structures.
[b] NPA charges (e).
[c] RMSD was calculated only with heavy atoms of the respective structures.

tively, in an AA9 LPMO with a similar ASM approach (11). Interestingly, the charge distribution of the coordinating histidine residues does not show a significant change, despite the substantial change in the copper ion oxidation state. This result suggests that the LPMO active site is able to readily accommodate both oxidation states of copper with little overall change in the charge distribution in the enzyme.

DISCUSSION

The present study presents the second structure of a CBM33 with copper bound and the first structure of a CBM33 with a Cu(II) ion. Using a data collection strategy allowing for the structure determination of LPMO structures in both copper oxidation states, we were able to visualize structural and copper coordination changes associated with reduction. This experimental methodology is quite generalizable and can be used to capture the electronic and structural transitions in metalloenzyme reduction at advanced light sources.

It has been proposed that an electron from cellobiose dehydrogenase or from a small molecule reducing agent such as
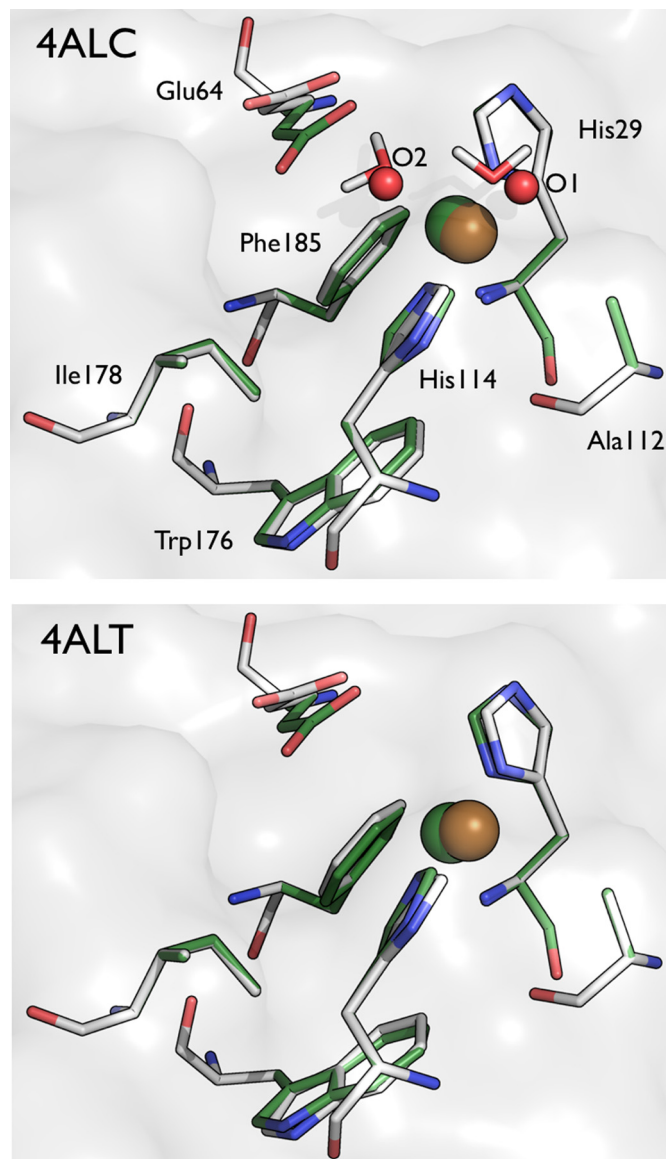

FIGURE 4. **Comparison of the crystallographically determined active sites of 4ALC (*top panel*) and 4ALT (*bottom panel*) with quantum mechanically optimized active site models.** The residues in *gray* (carbon), *blue* (nitrogen), and *red* (oxygen) represent the crystal structures, and the residues shown in *green* represent the geometry optimized structures from the DFT calculations. The copper is colored *gold* and *green*, respectively. The water molecules from the crystal structure are shown as *red spheres* in 4ALC, and the optimized water molecules are shown in stick format.

ascorbic acid can reduce the LPMO copper ion to a formal oxidation state of Cu(I) (10), prior to binding of dioxygen. This order of events is in accordance with the notion that molecular oxygen tends to bind copper proteins when the metal ion is in the reduced monovalent state (59). Subsequent to dioxygen binding, the catalytic cycle is initiated, which results in substrate hydroxylation, followed by elimination to cleave the glycosidic linkage (10, 11). This general mechanism will incorporate a single oxygen atom from molecular oxygen into the products. The elimination product can then undergo a hydrolysis reaction, which will incorporate an oxygen atom from water, as demonstrated in the mass spectrometry experiments performed by Vaaje-Kolstad *et al.* (6) with CBP21 and ^{18}O-containing reagents. Interestingly, the series of structures

TABLE 6
LPMO active site geometries and the likely oxidation state of the metal ion based on the coordination number and molecular geometry

Protein	PDB ID	Chain ID	Metal	Geometry[a]	CN
*Efa*CBM33	4ALC	A	Cu^{2+}	*tbp*	5
*Efa*CBM33	4ALT	A	Cu^{+}	*Tsh*	3
*Sma*CBP21	2BEM	A			
	2BEM	B			
	2BEM	C	Na^{+}	*sqpl*	4
*Bam*CBM33	2YOX	A	Cu^{+}	*Tsh*	3
		B	Cu^{+}	*Tsh*	3
	2YOY	A	Cu^{+}	*Tsh*	3
		B	Cu^{+}	*Tsh*	3
*Pch*GH61D	4B5Q	A	Cu^{2+}	O_h	6^b
		B	Cu^{2+}	O_h	6^b
*Ncr*PMO-2	4EIR	A	Cu^{2+}	O_h	6
		B	Cu^{2+}	O_h	6
*Ncr*PMO-3	4EIS	A	Cu^{2+}	O_h	6^c
		B	Cu^{2+}	*sqpy*	5
*Tte*GH61E-1	3EII	A	Zn^{2+}	O_h	6
		B	Zn^{2+}	O_h	6
		C	Zn^{2+}	O_h	6
		D	Zn^{2+}	*sqpy*	5
*Tte*GH61E-2	3EJA	A	Mg^{2+}	*sqpy*	6^d
		B	Mg^{2+}	*tbp*	5^e
		C	Mg^{2+}	*sqpy*	5
		D	Mg^{2+}	*sqpy*	5
*Hje*GH61B	2VTC	A	Ni^{2+}	O_h	6^f
		B	Ni^{2+}	O_h	6
*Tau*GH61A	2YET[g]	A	Cu^{2+}	O_h	6
		B	Cu^{2+}	O_h	6
*Tau*GH61A	3ZUD[h]	A	Cu^{2+}		
*Ao*AA11	4MAH	A	Zn^{2+}	*Tsh*	3
	4MAI	A	Cu^{2+}	*Tsh*	3

[a] *tbp*, trigonal bipyrimidal; *Tsh*, T-shaped; O_h, octahedral; *sqpl*, square planar; *sqpy*, square pyramidal.
[b] A glycerol molecule coordinates the two positions around the copper ion; it is not modeled as such.
[c] Long distances to O 3.6 Å and superoxide 3.44 Å.
[d] Coordinates an SO_4^{2-} at 4.1 Å.
[e] Coordinates an SO_4^{2-} at 4.1 Å.
[f] One oxygen ligand at 1.21 Å.
[g] Copper ions modeled with 20% occupancy.
[h] Copper modeled in dual conformations, partly surrounded by unmodeled density and a glycerol.

described in the present study show very little structural variation in the conformation of the copper site, despite the change in the copper coordination state induced by x-ray photoreduction. This result highlights that the LPMO catalytic center is preorganized to readily accommodate both oxidation states of copper.

Building on the present results, including the use of the CSD to "annotate" copper site configurations, we conducted a survey of previously reported LPMO structures in terms of their copper oxidation state, the results of which are reported in Table 6. The structures that are annotated as having a Cu(II) metal, *Ncr*PMO-2, *Ncr*PMO-3, and *Tau*GH61A, all exhibit an octahedral six-coordinated octahedral binding motif, which is compatible with the copper being Cu(II). Although the variation in bond lengths and angles is quite high between noncrystallographic symmetry-related molecules in some structures, as well as between the different structures, it is reasonable to conclude that all these published structures represent oxidized Cu(II), in accordance with annotation in the PDB. It is interesting to note that known AA9 LPMO structures with copper contain Cu(II), even though specific precautions to prevent x-ray photoreduction do not seem to have been taken. Under standard x-ray conditions, photoreduction of copper bound to CBM33s readily takes place (27), which could indicate a difference between the AA9 and AA10 LPMO copper sites, possibly caused by the extra coordinating tyrosine in AA9 LPMOs (Fig. 3*b*). Indeed, based on observed structural and EPR-spectrum differences, Hemsworth *et al.* (27) have suggested that the oxidative chem-

istries catalyzed by these enzyme families may differ. Further work is needed to substantiate this hypothesis. Regardless, considering the large overall similarity of the copper sites (Fig. 3), including the histidine brace, it seems reasonable to hypothesize that both enzyme types employ similar catalytic activation steps for reduction of the copper atom to prime the active site for binding molecular oxygen. Thus, it is likely that the structural and electronic insight obtained here for an AA10 LPMO will be relatively similar for an AA9 LPMO enzyme.

Lastly, the DFT calculations employed here reveal that primarily a coordination number change with only very minor geometry changes in the coordinating atoms is required for binding to the copper ion as it goes from a Cu(II) state to Cu(I). As measured by the atomic charges, very little change occurs in the surrounding protein residues electronically. This result is similar to that found for an AA9 LPMO in our recent mechanistic study (11). Therein, we computed the partial charges of the *Thermoauscus aurantiacus* AA9 LPMO (*Tau*GH61A) upon copper reduction from Cu(II) to Cu(I) as the step before oxygen binding. This calculation showed that the partial charges of the coordinating atoms only very slightly change upon reduction and concomitant removal of the coordinating water molecules, which in an AA9 LPMO changes the copper coordination from distorted octahedral to tetrahedral coordination (11). Taken together, these results suggest that both fungal and nonfungal LPMO active sites are quite plastic and can readily bind both states of copper. Moreover, the development of a robust ASM for AA10 LPMOs will likely enable the study of

the complete reaction mechanism of this family of LPMOs using a cluster model or theozyme approach, similar to that done for AA9 LPMOs (11).

CONCLUSIONS

In this study, we present a crystallographic and computational study of the effects of copper reduction in *Efa*CBM33, using the structures of well characterized small molecule copper complexes from the CSD to assign the oxidation state the copper ion. X-ray photoreduction causes clear changes in the active site of *Efa*CBM33, namely the loss of the coordinating water molecules. By correlating the structural data with the CSD, the two forms of *Efa*CBM33A were assigned as a Cu(II) and Cu(I) state with a trigonal bipyramidal and T-shaped geometry, respectively. DFT calculations reveal only minor changes in the atomic charges required for binding to either oxidation state of the copper ion, similar to what was found in a theoretical study for an AA9 LPMO (11). This study provides the first experimental data set to provide insight in the reductive step that activates an LPMO for catalysis.

REFERENCES

1. Chundawat, S. P., Beckham, G. T., Himmel, M. E., and Dale, B. E. (2011) Deconstruction of lignocellulosic biomass to fuels and chemicals. *Annu. Rev. Chem. Biomol. Eng.* **2,** 121–145
2. Himmel, M. E., Ding, S. Y., Johnson, D. K., Adney, W. S., Nimlos, M. R., Brady, J. W., and Foust, T. D. (2007) Biomass recalcitrance: engineering plants and enzymes for biofuels production. *Science* **315,** 804–807
3. Eijsink, V. G., Vaaje-Kolstad, G., Vårum, K. M., and Horn, S. J. (2008) Towards new enzymes for biofuels: lessons from chitinase research. *Trends Biotechnol.* **26,** 228–235
4. Cantarel, B. L., Coutinho, P. M., Rancurel, C., Bernard, T., Lombard, V., and Henrissat, B. (2009) The Carbohydrate-Active EnZymes database (CAZy): an expert resource for Glycogenomics. *Nucleic Acids Res.* **37,** D233–D238
5. Levasseur, A., Drula, E., Lombard, V., Coutinho, P. M., and Henrissat, B. (2013) Expansion of the enzymatic repertoire of the CAZy database to integrate auxiliary redox enzymes. *Biotechnol. Biofuels* **6,** 41
6. Vaaje-Kolstad, G., Westereng, B., Horn, S. J., Liu, Z., Zhai, H., Sørlie, M., and Eijsink, V. G. (2010) An oxidative enzyme boosting the enzymatic conversion of recalcitrant polysaccharides. *Science* **330,** 219–222
7. Quinlan, R. J., Sweeney, M. D., Lo Leggio, L., Otten, H., Poulsen, J. C., Johansen, K. S., Krogh, K. B., Jørgensen, C. I., Tovborg, M., Anthonsen, A., Tryfona, T., Walter, C. P., Dupree, P., Xu, F., Davies, G. J., and Walton, P. H. (2011) Insights into the oxidative degradation of cellulose by a copper metalloenzyme that exploits biomass components. *Proc. Natl. Acad. Sci. U.S.A.* **108,** 15079–15084
8. Forsberg, Z., Vaaje-Kolstad, G., Westereng, B., Bunaes, A. C., Stenstrøm, Y., MacKenzie, A., Sørlie, M., Horn, S. J., and Eijsink, V. G. (2011) Cleavage of cellulose by a CBM33 protein. *Protein Sci.* **20,** 1479–1483
9. Westereng, B., Ishida, T., Vaaje-Kolstad, G., Wu, M., Eijsink, V. G., Igarashi, K., Samejima, M., Ståhlberg, J., Horn, S. J., and Sandgren, M. (2011) The putative endoglucanase PcGH61D from *Phanerochaete chrysosporium* is a metal-dependent oxidative enzyme that cleaves cellulose. *PLoS One* **6,** e27807
10. Phillips, C. M., Beeson, W. T., Cate, J. H., and Marletta, M. A. (2011) Cellobiose dehydrogenase and a copper-dependent polysaccharide monooxygenase potentiate cellulose degradation by *Neurospora crassa*. *ACS Chem. Biol.* **6,** 1399–1406
11. Kim, S., Ståhlberg, J., Sandgren, M., Paton, R. S., and Beckham, G. T. (2014) Quantum mechanical calculations suggest that lytic polysaccharide monooxygenases use a copper-oxyl, oxygen-rebound mechanism. *Proc. Natl. Acad. Sci. U.S.A.* **111,** 149–154
12. Hemsworth, G. R., Henrissat, B., Davies, G. J., and Walton, P. H. (2014) Discovery and characterization of a new family of lytic polysaccharide monooxygenases. *Nat. Chem. Biol.* **10,** 122–126
13. Harris, P. V., Welner, D., McFarland, K. C., Re, E., Navarro-Poulsen, J. C., Brown, K., Salbo, R., Ding, H., Vlasenko, E., Merino, S., Xu, F., Cherry, J., Larsen, S., and Lo Leggio, L. (2010) Stimulation of lignocellulosic biomass hydrolysis by proteins of glycoside hydrolase family 61: structure and function of a large, enigmatic family. *Biochemistry* **49,** 3305–3316
14. Horn, S. J., Vaaje-Kolstad, G., Westereng, B., and Eijsink, V. G. (2012) Novel enzymes for the degradation of cellulose. *Biotechnol. Biofuels* **5,** 45
15. Merino, S., and Cherry, J. (2007) Progress and challenges in enzyme development for biomass utilization. In *Biofuels* (Olsson, L., ed) pp. 95–120, Springer, Berlin
16. Beckham, G. T., and Crowley, M. F. (2011) Examination of the α-chitin structure and decrystallization thermodynamics at the nanoscale. *J. Phys. Chem. B* **115,** 4516–4522
17. Beckham, G. T., Matthews, J. F., Peters, B., Bomble, Y. J., Himmel, M. E., and Crowley, M. F. (2011) Molecular-level origins of biomass recalcitrance: decrystallization free energies for four common cellulose polymorphs. *J. Phys. Chem. B* **115,** 4118–4127
18. Payne, C. M., Himmel, M. E., Crowley, M. F., and Beckham, G. T. (2011) Decrystallization of oligosaccharides from the cellulose Iβ surface with molecular simulation. *J. Phys. Chem. Lett.* **2,** 1546–1550
19. Aachmann, F. L., Sørlie, M., Skjåk-Braek, G., Eijsink, V. G., and Vaaje-Kolstad, G. (2012) NMR structure of a lytic polysaccharide monooxygenase provides insight into copper binding, protein dynamics, and substrate interactions. *Proc. Natl. Acad. Sci. U.S.A.* **109,** 18779–18784
20. Isaksen, T., Westereng, B., Aachmann, F. L., Agger, J. W., Kracher, D., Kittl, R., Ludwig, R., Haltrich, D., Eijsink, V. G., and Horn, S. J. (2014) A C4-oxidizing lytic polysaccharide monooxygenase cleaving both cellulose and cello-oligosaccharides. *J. Biol. Chem.* **289,** 2632–2642
21. Vaaje-Kolstad, G., Horn, S. J., van Aalten, D. M., Synstad, B., and Eijsink, V. G. (2005) The non-catalytic chitin-binding protein CBP21 from *Serratia marcescens* is essential for chitin degradation. *J. Biol. Chem.* **280,** 28492–28497
22. Vaaje-Kolstad, G., Houston, D. R., Riemen, A. H., Eijsink, V. G., and van Aalten, D. M. (2005) Crystal structure and binding properties of the *Serratia marcescens* chitin-binding protein CBP21. *J. Biol. Chem.* **280,** 11313–11319
23. Bøhle, L. A., Mathiesen, G., Vaaje-Kolstad, G., and Eijsink, V. G. (2011) An endo-ss-*N*-acetylglucosaminidase from *Enterococcus faecalis* V583 responsible for the hydrolysis of high-mannose and hybrid-type N-linked glycans. *FEMS Microbiol. Lett.* **325,** 123–129
24. Vaaje-Kolstad, G., Bøhle, L. A., Gåseidnes, S., Dalhus, B., Bjørås, M., Mathiesen, G., and Eijsink, V. G. (2012) Characterization of the chitinolytic machinery of *Enterococcus faecalis* V583 and high-resolution structure of its oxidative CBM33 enzyme. *J. Mol. Biol.* **416,** 239–254
25. Vebø, H. C., Snipen, L., Nes, I. F., and Brede, D. A. (2009) The transcriptome of the nosocomial pathogen *Enterococcus faecalis* V583 reveals adaptive responses to growth in blood. *PLoS One* **4,** e7660
26. Vebø, H. C., Solheim, M., Snipen, L., Nes, I. F., and Brede, D. A. (2010) Comparative genomic analysis of pathogenic and probiotic *Enterococcus faecalis* isolates, and their transcriptional responses to growth in human urine. *PLoS One* **5,** e12489
27. Hemsworth, G. R., Taylor, E. J., Kim, R. Q., Gregory, R. C., Lewis, S. J., Turkenburg, J. P., Parkin, A., Davies, G. J., and Walton, P. H. (2013) The copper active site of CBM33 polysaccharide oxygenases. *J. Am. Chem. Soc.* **135,** 6069–6077
28. Wu, M., Beckham, G. T., Larsson, A. M., Ishida, T., Kim, S., Payne, C. M., Himmel, M. E., Crowley, M. F., Horn, S. J., Westereng, B., Igarashi, K., Samejima, M., Ståhlberg, J., Eijsink, V. G., and Sandgren, M. (2013) Crystal structure and computational characterization of the lytic polysaccharide monooxygenase GH61D from the basidiomycota fungus *Phanerochaete chrysosporium*. *J. Biol. Chem.* **288,** 12828–12839
29. Beeson, W. T., Phillips, C. M., Cate, J. H., and Marletta, M. A. (2012)

Oxidative cleavage of cellulose by fungal copper-dependent polysaccharide monooxygenases. *J. Am. Chem. Soc.* **134,** 890–892

30. Vu, V. V., Beeson, W. T., Phillips, C. M., Cate, J. H., and Marletta, M. A. (2014) Determinants of regioselective hydroxylation in the fungal polysaccharide monooxygenases. *J. Am. Chem. Soc.* **136,** 562–565

31. Allen, F. H. (2002) The Cambridge Structural Database: a quarter of a million crystal structures and rising. *Acta Crystallogr. B* **58,** 380–388

32. McGeehan, J., Ravelli, R. B., Murray, J. W., Owen, R. L., Cipriani, F., McSweeney, S., Weik, M., and Garman, E. F. (2009) Colouring cryo-cooled crystals: online microspectrophotometry. *J. Synchrotron Radiat.* **16,** 163–172

33. Flot, D., Mairs, T., Giraud, T., Guijarro, M., Lesourd, M., Rey, V., van Brussel, D., Morawe, C., Borel, C., Hignette, O., Chavanne, J., Nurizzo, D., McSweeney, S., and Mitchell, E. (2010) The ID23–2 structural biology microfocus beamline at the ESRF. *J. Synchrotron Radiat.* **17,** 107–118

34. Adam, V., Royant, A., Nivière, V., Molina-Heredia, F. P., and Bourgeois, D. (2004) Structure of superoxide reductase bound to ferrocyanide and active site expansion upon x-ray-induced photo-reduction. *Structure* **12,** 1729–1740

35. Kabsch, W. (2010) XDS. *Acta Crystallogr. D Biol. Crystallogr.* **66,** 125–132

36. Bailey, S. (1994) The Ccp4 Suite: programs for protein crystallography. *Acta Crystallogr. D* **50,** 760–763

37. Emsley, P., and Cowtan, K. (2004) Coot: model-building tools for molecular graphics. *Acta Crystallogr. D* **60,** 2126–2132

38. Murshudov, G. N., Vagin, A. A., and Dodson, E. J. (1997) Refinement of macromolecular structures by the maximum-likelihood method. *Acta Crystallogr. D* **53,** 240–255

39. DeLano, W. L. (2002) *The PyMOL Molecular Graphics System*, DeLano Scientific, San Carlos, CA

40. Kleywegt, G. J. (1996) Use of non-crystallographic symmetry in protein structure refinement. *Acta Crystallogr. D Biol. Crystallogr.* **52,** 842–857

41. Kleywegt, G. J., and Jones, T. A. (1996) Phi/psi-chology: Ramachandran revisited. *Structure* **4,** 1395–1400

42. Echols, N., Grosse-Kunstleve, R. W., Afonine, P. V., Bunkóczi, G., Chen, V. B., Headd, J. J., McCoy, A. J., Moriarty, N. W., Read, R. J., Richardson, D. C., Richardson, J. S., Terwilliger, T. C., and Adams, P. D. (2012) Graphical tools for macromolecular crystallography in PHENIX. *J. Appl. Crystallogr.* **45,** 581–586

43. Murray, J. W., Garman, E. F., and Ravelli, R. B. (2004) X-ray absorption by macromolecular crystals: the effects of wavelength and crystal composition on absorbed dose. *J. Appl. Crystallogr.* **37,** 513–522

44. Paithankar, K. S., Owen, R. L., and Garman, E. F. (2009) Absorbed dose calculations for macromolecular crystals: improvements to RADDOSE. *J. Synchrotron Radiat.* **16,** 152–162

45. Frisch, M. J., Trucks, G. W., Schlegel, H. B., Scuseria, G. E., Robb, M. A., Cheeseman, J. R., Scalmani, G., Barone, V., Mennucci, B., and Petersson, G. A. (2010) *Gaussian 09*, revision B. 01. Gaussian, Inc., Wallingford, CT

46. Dechancie, J., Clemente, F. R., Smith, A. J., Gunaydin, H., Zhao, Y.-L., Zhang, X., and Houk, K. N. (2007) How similar are enzyme active site geometries derived from quantum mechanical theozymes to crystal structures of enzyme-inhibitor complexes? Implications for enzyme design. *Protein Sci.* **16,** 1851–1866

47. Zhao, Y., and Truhlar, D. (2008) The M06 suite of density functionals for main group thermochemistry, thermochemical kinetics, noncovalent interactions, excited states, and transition elements: two new functionals and systematic testing of four M06-class functionals and 12 other functionals. *Theor. Chem. Account* **120,** 215–241

48. Zhao, Y., and Truhlar, D. G. (2008) Density functionals with broad applicability in chemistry. *Acc. Chem. Res.* **41,** 157–167

49. Barone, V., and Cossi, M. (1998) Quantum calculation of molecular energies and energy gradients in solution by a conductor solvent model. *J. Phys. Chem. A* **102,** 1995–2001

50. Cossi, M., Rega, N., Scalmani, G., and Barone, V. (2003) Energies, structures, and electronic properties of molecules in solution with the C-PCM solvation model. *J. Comput. Chem.* **24,** 669–681

51. Liao, R.-Z., and Thiel, W. (2013) On the effect of varying constraints in the quantum mechanics only modeling of enzymatic reactions: the case of acetylene hydratase. *J. Phys. Chem. B* **117,** 3954–3961

52. Terwilliger, T. C., Grosse-Kunstleve, R. W., Afonine, P. V., Moriarty, N. W., Adams, P. D., Read, R. J., Zwart, P. H., and Hung, L. W. (2008) Iterative-build OMIT maps: map improvement by iterative model building and refinement without model bias. *Acta Crystallogr. D Biol. Crystallogr.* **64,** 515–524

53. Matthews, B. W. (1968) Solvent content of protein crystals. *J. Mol. Biol.* **33,** 491–497

54. Hemsworth, G. R., Davies, G. J., and Walton, P. H. (2013) Recent insights into copper-containing lytic polysaccharide mono-oxygenases. *Curr. Opin. Struct. Biol.* **23,** 660–668

55. Karkehabadi, S., Hansson, H., Kim, S., Piens, K., Mitchinson, C., and Sandgren, M. (2008) The first structure of a glycoside hydrolase family 61 member, Cel61B from *Hypocrea jecorina*, at 1.6 angstrom resolution. *J. Mol. Biol.* **383,** 144–154

56. Li, X., Beeson, W. T., 4th, Phillips, C. M., Marletta, M. A., and Cate, J. H. (2012) Structural basis for substrate targeting and catalysis by fungal polysaccharide monooxygenases. *Structure* **20,** 1051–1061

57. Casella, L., Carugo, O., Gullotti, M., Doldi, S., and Frassoni, M. (1996) Synthesis, structure, and reactivity of model complexes of copper nitrite reductase. *Inorg. Chem.* **35,** 1101–1113

58. Sorrell, T. N., Garrity, M. L., Richards, J. L., and White, P. S. (1994) Synthesis, structural characterization and dioxygen reactivity of imidazole-ligated Cu (I) complexes. *Inorg. Chim. Acta* **218,** 103–108

59. Que, L., Jr., and Tolman, W. B. (2008) Biologically inspired oxidation catalysis. *Nature* **455,** 333–340